On the Feasibility of RIS-enabled Cooperative Driving

Michele Segata*, Paolo Casari*, Marios Lestas†, Dimitrios Tyrovolas‡, Taqwa Saeed§, George Karagiannidis‡¶, Christos Liaskos‖

*Department of Information Engineering and Computer Science – University of Trento, Italy
†Dept. of Electrical Engineering – Frederick University, Cyprus
‡Dept. of Electrical Engineering – Aristotle University of Thessaloniki, Greece
§School of Information Technology – Halmstad University, Sweden
¶Cyber Security Systems and Applied AI Research Center, Lebanese American University (LAU), Lebanon
‖Dept. of Computer Science and Engineering – University of Ioannina & FORTH, Greece

***Abstract*—Future cooperative autonomous vehicles will require high-performance communication means to support functions such as cooperative maneuvering and cooperative perception. The high-bandwidth requirements of these functions can be met through mmWave communications, whose utilization is often hindered by the harsh propagation conditions of typical vehicular environments. A solution to this problem is the use of reconfigurable intelligent surfaces (RISs), which enable the reflection of signals in a configurable direction, and have recently gained attention in the vehicular domain. In this paper, we provide an initial feasibility study, highlighting the challenges ahead and the performance RISs need to deliver in order to enable this type of communications. Specifically, we utilize CoopeRIS, a simulation framework for RISs integrated into the Plexe/Veins/SUMO ecosystem that we develop as further contribution and will release to the public.**

I. Introduction and Related Work

Car accidents and traffic congestion have been identified as significant obstacles for the smart city paradigm, yielding human deaths and economic losses [1]. Cooperative autonomous vehicles (CAVs) constitute a promising solution [2], as they perceive their environment and roadway conditions, and adapt to them by performing reliable driving functions. However, CAVs require an underlying, highly-dependable and high-performance wireless communication infrastructure. Applications that can benefit from such infrastructure include cooperative driving and perception, vehicular edge computing (VEC), and distributed learning. In this context, mmWave communications have been well established to serve cooperative vehicular applications due to their high-bandwidth performance [3], but are prone to strong signal attenuation in the presence of blocking bodies, e.g., around buildings and intersections [4]. The unpredictable appearance of blockage and the temporary disconnection that ensue may thus prevent mmWave technology from delivering the dependable, high-bandwidth, and low-delay communications that cooperative vehicular applications require.

Recently, a new wireless communication paradigm named programmable wireless environments (PWEs) has emerged, which strives to constitute the wireless propagation phenomenon into a fully controllable process, and thus mitigate previously unmanageable phenomena [5]. To realize this, PWEs coat the environment's planar objects with metasurfaces supporting well-defined networking and programming interfaces, denoted as reconfigurable intelligent surfaces (RISs). RISs can passively alter the power, direction, polarization, and phase of any impinging wave by tuning the impedance of their reflecting elements [6]. In a popular RIS implementation, such tuning is achieved through varactors and varistors, or by constructing the reflecting elements from appropriate materials, e.g., liquid crystals. In either case, the objective is to provide a desired scattering diagram [7], [8]. Multiple deployed RISs can be dynamically orchestrated to realize custom end-to-end wireless propagation routes between vehicles, e.g., bypassing obstacles and offering a virtual line-of-sight link, thus enhancing the quality and reliability of the channel [9].

RISs have been considered in a number of recent works targeting vehicular communication scenarios [10], focusing mostly on preserving reliability under fast mobility. For example, a robust transmission scheme for RIS-assisted vehicular communication was proposed in [11], while the works in [12] and [13] derived the performance of a vehicular RIS-assisted network in terms of outage probability and security. Moreover, the authors in [14] optimized RIS placement to maximize the received power for a communication scenario between a base station and an autonomous vehicle, while in [15] the authors investigated communication aspects that can affect the vehicular network, such as configuration delays and power consumption. Finally, the authors of [16] developed a simulation framework that complements autonomous driving with realistic vehicular mobility models and networking features, and embeds RISs coding and gain models. Nevertheless, the aforementioned framework can only provide results for single RIS scenarios, which greatly limits the PWE effectiveness [17].

The present paper contributes: i) a feasibility study and exploration of the RIS/autonomous driving synergy in the mmWave band deriving important insights especially relevant for vehicle-to-vehicle communications (V2V) in the design

phase, and ii) a sophisticated simulation framework called CoopeRIS which supports multiple RISs and accounts for their structural characteristics, i.e., the number and density of their radiating elements. The framework will be open to the public, and is compatible with the popular Plexe/Veins/SUMO ecosystem [18]. The algorithmic workflow of the simulator, as well as the supported wireless channel modeling options are presented in details, followed by a use-case study on challenging intersection scenarios.

The remainder of the paper is organized as follows. Section II-B details the supported RIS-enabled communication models and their implementation in the framework. Section III describes the simulated scenarios, while Section IV discusses the results. Finally, we draw concluding remarks in Section V.

II. Communication Models

A. RIS model

In this work we consider passive metasurfaces that operate according to the model presented in [19]. The aim of the surface is to focus an impinging signal from a certain incident angle towards a direction expressed as a reflection angle. Both the incidence and the reflection directions are defined using spherical coordinates, i.e., via pairs of angles (ϕ, θ) representing the azimuth and elevation, respectively. In real deployments, the duty of reconfiguring a surface to serve a specific pair of nodes belongs to a dedicated controller which receives instructions on a separate communication link, e.g., a cellular one. Here we disregard this aspect, assuming the controller can obtain the position of the vehicles at any required time.

Fig. 1 depicts the coordinate system. The elevation θ represents the angle between the direction vector and the vector normal to the surface, measured on the plane formed by the two vectors. When $\theta = 0°$, the direction vector is normal to the surface, whereas when $\theta = 90°$, the direction vector is parallel to it. The azimuth ϕ, instead, measures the rotation of the direction vector around the normal. This is obtained by projecting the direction vector on the plane of the surface and then measuring the angle between a reference direction representing $0°$.

The procedure to configure the metasurface is called coding. Its objective is to focus a signal coming from a given incident angle towards a chosen reflection angle. The coding procedure consists in finding the right phase shift for each of the unit cells. In [19], the possible number of phase shifts that can be assigned to a unit cell is discrete. Such value, defined as the number of unit cell states N_s, maps each state to a specific phase shift. For example, if $N_s = 4$, then the four states are mapped to phase shifts of $135°$, $45°$, $-45°$ and $135°$ (see [19, Fig. 4]). The larger N_s, the narrower the beam will become.

In addition to the number of coding states N_s, the model in [19] considers how many unit cells can be placed in the space of a wavelength (ρ_λ) and the size of the surface in multiples of the wavelength (N_λ). By default, the model considers a square surface, hence the total number of unit cells is $N_{el} = (\rho_\lambda \cdot N_\lambda)^2$. In the remainder of the paper, we use the terms *unit cells* and *reflecting elements* interchangeably.

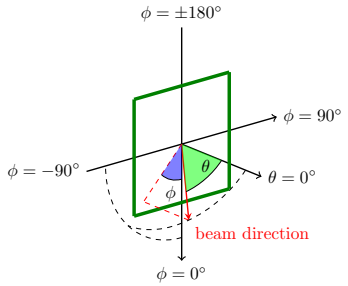

Figure 1. Graphical description of the coordinate system. The green square represents the metasurface.

After choosing the above parameters and after coding the metasurface for a specific pair of reflection and incidence angles, the model computes the far field pattern, i.e., the scattering diagram of the surface. This is a quad-dimensional map from the incidence and reflection angles to a real number, indicating indeed the gain. More formally, the far field pattern can be described as a function $f(\phi_r, \theta_r, \phi_i, \theta_i) \rightarrow \mathbb{R}$, where the subscripts r and i denote reflection and incidence angles, respectively. So far, the model in [19] considers a normal incidence, i.e., it is assumed that the incoming signal is always normal to the surface, so currently the far field pattern is described by $f(\phi_r, \theta_r, \phi_i = 0°, \theta_i = 0°) \rightarrow \mathbb{R}$. While the model of [19] studies only normal incidence, it is clarified that the same approach is generally applicable to any incidence angle, and we will extend it as part of our future work. We depict sample far field patterns in Section IV-A.

We implement the model in [19] in CoopeRIS to enable the computation of the gain of this specific RIS within the simulator. We do not detail the model here for the sake of brevity, as this is well-described in the original paper.

B. Channel model

To obtain a complete link budget equation, we need to consider the path loss incurred after multiple reflections, in addition to the gain provided by the RIS.

In the literature we find different path loss models for RIS [20], namely using the product or the sum of distances over the path. The application of one model or the other depends on the scenario. CoopeRIS implements both, so users can easily switch between them according to their scenario of interest.

We start by describing the channel model we will refer to as the "product of distances" model. In this model, each hop of the path is treated independent of the others, so that the free space path loss model is applied to each of them. In linear scale, this means computing the product of the path losses. The principle is that an emitter radiates the power in every direction, so that the free space path loss accounts for the amount of energy reaching the receiver as a function of distance. The RIS then behaves as if it was transmitting a new signal, again in every direction, with a transmission power that equals the received one. The directionality of the RIS is then modeled as a gain that depends on the incidence and reflection angles. This process repeats at each RIS till reaching the receiver.

More formally, we can describe such a model by defining the received power as:

$$P_r = \frac{P_t G_t G_r \prod_{i=1}^{N_{RIS}} G_i^{RIS}}{\prod_{i=1}^{N_{RIS}+1} \left(\frac{4\pi f}{c}\right)^2 d_i^{\alpha}}, \quad (1)$$

where P_t, G_t, and G_r represents the transmission power, the transmitter antenna gain, and the receiver antenna gain, respectively, f is the frequency and c the speed of light. N_{RIS} is the number of RISs, so $N_{RIS}+1$ is the number of hops along the full propagation path. G_i^{RIS} is the gain if the i-th RIS, d_i the i-th hop of the path and α the path loss exponent.

The channel model we refer to as "sum of distances" model considers the entire path as if it was a single hop. Thus, the path loss is computed using the free space formula with the total distance computed as the sum of the distance covered over each hop. According to the measurements in [20], this model applies only in special conditions, i.e., when operating in the near field of the RIS, so either very close to the surface or when the surface is very large. The received power in this case is defined as:

$$P_r = \frac{P_t G_t G_r \prod_{i=1}^{N_{RIS}} G_i^{RIS}}{\left(\frac{4\pi f}{c}\right)^2 \left(\sum_{i=1}^{N_{RIS}+1} d_i\right)^{\alpha}}. \quad (2)$$

C. Model implementation

This section presents the implementation of the model described in Section II-B within CoopeRIS, which is a discrete event simulation (DES) framework. It builds on top of the PLEXE, Veins, SUMO, and OMNeT++ ecosystem [18]. A preliminary version [16] only supported a single RIS, the sum of distances path loss model, and the metasurface could not be configured for different values of N_s, ρ_λ, and N_λ.

CoopeRIS implements a set of new modules for RIS-enabled mmWave channels, as well as a mmWave network interface card (NIC) with RIS capabilities. Such a NIC is used by both standard transceivers and RISs. The difference is that the NIC of transceivers includes both a MAC and a PHY layer module, whereas the NIC of RIS only includes a PHY layer. Currently, the MAC layer of the transceivers does not implement any channel access function, but just the encapsulation of data and encoding according to the required modulation and coding scheme (MCS). The PHY layer of RISs, on the other hand, only takes care of enacting reflections and marking frames with metadata necessary for the model.

When simulating classical transmissions in a DES, we just have to consider source/destination pairs. The application of the gain by a RIS, however, can only be done at the next hop, and requires knowledge of the previous hop, as the gain depends on the incidence and reflection angles. The PHY of a RIS is mainly responsible for reflecting an incoming signal, which is implemented by immediately retransmitting (i.e., with zero delay) a copy of the incoming signal and changing some of its properties, for example by setting a transmission power that matches the incoming one after applying the path loss and the gain of the previous RIS (if any). In addition, the module adds metadata to the frame such as, for example, the incidence angles, which are necessary for computing the gain at the next hop. The module also performs additional operations, such as avoiding infinite reflections or avoiding to reflect exceedingly low-power signals, for computational efficiency.

Listing 1 Incoming signal event handling. m represents the module executing the code, f is the incoming frame, d is the hop distance travelled by the frame.

```
1:  procedure onIncomingFrameStart(f, d)
2:      if f.srcType == NODE then                          ▷ frame from a node
3:          loss = (c/(4πf))^2 · 1/d^α
4:      else                                               ▷ frame from a RIS
5:          if use product of distances model then
6:              loss = (c/(4πf))^2 · 1/d^α
7:          else
8:              loss = (d_tot/(d_tot+d))^α
9:          (φ_r, θ_r) = angles(f.srcPos, m.pos)
10:         gain = f(φ_r, θ_r, f.φ_i, f.θ_i)
11:         loss = min(1, loss · gain)
12:     f.power = f.power × loss
13:     if m.isRIS then                                    ▷ this module is a RIS
14:         if f.power > δ and m ∉ f.risList then
15:             f.risList = f.risList ∪ {m}
16:             f.d_tot = f.d_tot + d
17:             (φ_i, θ_i) = angles(f.srcPos, m.pos)
18:             f.φ_i = φ_i
19:             f.θ_i = θ_i
20:             f.srcType = RIS
21:             transmit(f)
22: procedure onIncomingFrameEnd(f)
23:     if not m.isRIS then
24:         if attemptDecoding(f) == SUCCESS then
25:             sendToMAC(f)
```

With the help of the pseudocode in Listing 1, we now describe the handling of an incoming frame event in the simulator, which is basically the core part of CoopeRIS. The pseudocode considers a frame to be an object with a set of properties: *power*, *srcType*, *srcPos*, ϕ_i, θ_i, *risList*, and d_{tot}. Power indicates the signal power at which the frame was transmitted, so prior to the application of the path loss models. This is standard in network DES, as the path loss depends on the receiver and so it is applied on reception. The attributes *srcType* and *srcPos* indicate the type (standard transceiver node or RIS) and the position of the transmitter. ϕ_i and θ_i indicate the incidence azimuth and elevation, which are added as metadata by a RIS object before retransmitting the signal, so that the next hop can properly compute the gain[1]. *risList* indicates the list of RISs that have reflected the signal, while d_{tot} indicates the distance traveled by the signal so far.

We start now describing Listing 1. The pseudocode comprises two methods: onIncomingFrameStart and onIncomingFrameEnd. They correspond to the beginning and end of the signal reception events. onIncomingFrameStart has two parameters, the frame f and the hop distance d. The simulator first checks whether the frame comes from a standard transceiver node or a RIS. If the signal comes from a node, then this is necessarily the first hop, so the power is reduced according to free space path loss. If otherwise the signal comes from a RIS (Line 4) then we first compute the amount of loss

[1]As described before, the incidence direction has currently no effect, but it is already implemented in the simulator for the future extensions we plan.

to be applied. If we use the product of distances model, we simply apply the free space path loss computed over the hop distance d, otherwise we apply a loss of $\left(\frac{d_{tot}}{d_{tot}+d}\right)^{\alpha}$. This factor is obtained by considering that, under the sum of distances model, the power at the n-th hop should be

$$P_n = P_t \cdot \left(\frac{c}{4\pi f}\right)^2 \cdot \left(\frac{1}{d_1 + \cdots + d_n}\right)^{\alpha} \tag{3}$$

The attenuation factor between hops $n-1$ and n is easily obtained by computing

$$\frac{P_n}{P_{n-1}} = \left(\frac{d_1 + \cdots + d_{n-1}}{d_1 + \cdots + d_{n-1} + d_n}\right)^{\alpha} = \left(\frac{d_{tot}}{d_{tot} + d}\right)^{\alpha}. \tag{4}$$

The next step (Line 9) is to compute the gain due to the previous RIS. We thus compute the reflection azimuth and elevation angles ϕ_r and θ_r and obtain the gain from the far field model $f(\phi_r, \theta_r, \phi_i, \theta_i)$. Next (Line 11), we make sure that the RIS does not violate the law of conservation of energy by checking that the gain is at maximum 1. When being very close to the RIS it might happen that the gain is larger than the loss, so we simply make sure that the RIS can emit at most the same amount of energy that it received because we consider a passive metasurface. Finally, we apply the computed loss to the power of the incoming frame.

After applying the gain/path loss models, if the receiving module is a RIS we might need to retransmit the signal (Line 13). First, the signal is only retransmitted if the received power is larger than a certain threshold δ. If the power is too low, there is no chance receivers will be able to decode the frame after reflecting it, regardless of the gain of the RIS (again, the metasurface we consider is passive). This is common practice in DES and enhances the efficiency of the simulator. The threshold needs to be chosen properly to avoid underestimating interference in multi-access scenarios. The second condition checks that the current RIS has not already reflected such signal before, to avoid infinite reflections. If the conditions are met, then we update the list of RISs that have reflected the signal, as well as the total distance travelled. We compute the incidence azimuth and elevation that will be necessary for computing the RIS gain at the next hop, set the source type, and finally retransmit the frame.

Notice that here there is no decoding attempt, as such event is triggered at the beginning of a reception. Decoding is attempted instead at the end of the reception, i.e., when the ONINCOMINGFRAMEEND event is triggered. Decoding is only attempted by standard transceiver nodes and, if successful, the received frame is sent up the protocol stack.

III. SIMULATION SCENARIOS

To analyze the feasibility of RIS-enabled V2V communications and to show the potential of CoopeRIS towards the design and the performance evaluation of such systems, we devise two scenarios, both comprising intersections with shadowing caused by buildings. One scenario considers a T-shaped intersection with a single RIS, while the other includes two intersections with two reflections, as shown in Fig. 2. We will refer to the

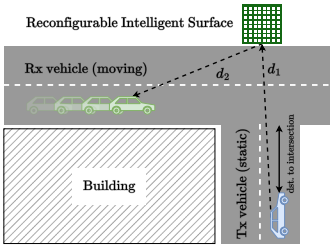

(a) T-intersection scenario

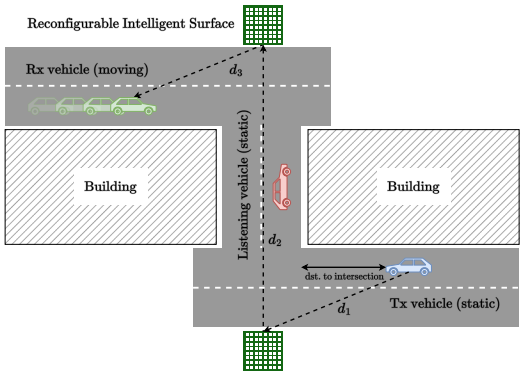

(b) Z-intersection scenario

Figure 2. Scenarios implemented in the simulator.

second scenario as the Z-shaped scenario. The length of the vertical road of the Z scenario is $60\,\mathrm{m}$. RISs are located directly at the intersection and are placed $10\,\mathrm{m}$ above the ground.

In both cases, we consider a static transmitter located at different distances from the intersection, and a receiver moving towards the intersection. The RIS is coded so that the incidence angle matches the location of the static transmitter. In the T scenario, the RIS points the reflected signal towards the receiver, whereas in the Z scenario the first RIS points towards the second one, the incidence angle of the second RIS is configured to focus the beam coming from the first RIS and to reflect the signal towards the receiver. For each scenario, we consider two sub-scenarios, i.e., *tracking* and *no tracking*. In the first one, the RIS perfectly tracks the receiver, reconfiguring itself for each signal to be delivered. In the second one, instead, the RIS is statically preconfigured to point the reflected signal $50\,\mathrm{m}$ before the intersection. With the T and Z scenarios, we aim at understanding the impact of single and multiple reflections, while sub-scenarios allow us to evaluate to which extent perfect tracking of the receivers is necessary and whether a static configuration might suffice.

In the simulation, we consider different RIS sizes, hence ultimately a different total number of elements. In the tracking scenario, we consider 625 and 2500 elements, while in the no-tracking scenario we span a minimum of 625 up to a maximum of $10\,000$ elements. Note that we limit the maximum number of elements in the tracking scenario because of the computational complexity of the reconfiguration process. So far, the algorithm is not yet optimized, making continuous reconfiguration unfeasible. In the no tracking scenario, the RIS is configured once for the whole simulation, enabling us to

Table I
SIMULATION PARAMETERS.

Parameter	Value
Path loss model	Free space ($\alpha = 2.0$), with sum and product of distances
Shadowing model	Simple obstacle shadowing [21]
RIS gain G^{RIS}	Far field model derived from [19]
Antenna gains G_t and G_r	1 (isotropic radiator)
Frequency	25 GHz
Transmit power	30 dBm
Txer distance to inters.	0, 5, 10, 15, 20, 25, 50, 75, 100, 150, and 200 m
Coding states (N_s)	8
Elements per λ (ρ_λ)	5
RIS N_λ (tracking)	$5, 10$ λ
N_{el} (tracking)	625, 2500
RIS N_λ (no tracking)	$5, 6, 7, 8, 9, 10, 12, 15, 18, 20$ λ
N_{el} (no tracking)	625, 900, 1225, 1600, 2025, 2500, 3600, 5625, 8100, 10000

explore a larger parameter set.

Finally, in the Z scenario, we consider an additional receiving vehicle placed in the middle of the vertical road to measure the feasibility of having multiple receivers without the need of reconfiguring the RISs. This might be of interest in VEC scenarios, where we need to transfer data towards multiple computing nodes (in this case, vehicles). Table I summarizes simulation parameters.

IV. Results and analysis

A. Impact of the number of element in a RIS

As a first result we show the far field patterns of the RIS model for different number of elements N_{el}. This clarifies the impact of N_{el} on the gain of the metasurface and on the properties of its beam pattern, and provides the necessary background for the results in the following sections. By implementing the model in [19] within CoopeRIS, we can generate and visualize the far field pattern of the metasurface, which is expressed by a gain that depends on the incidence and reflection azimuth and elevation angles. For the analysis, we code the metasurface for $\phi_r = -45°, \theta_r = 45°, \phi_i = 0°, \theta_i = 0°$, $N_s = 8$, and for a number of elements N_{el} equal to 625, 2500, 10 000. Fig. 3 shows the results in terms of gain for different values of N_{el}, in linear and logarithmic scale.

The results in linear scale effectively show that metasurfaces with a higher number of elements focuses more energy towards the direction of reflection, both by reducing the size of the beam and by increasing its maximum gain. Note that whether or not a configuration can be deemed better than the others depends on whether broader coverage or higher gain is desired, which in turn depends on the application requirements and on the scenario under investigation (see the analysis in the next sections). In addition, the actual coverage area depends on the distance from the surface: a narrow beam can still cover a large portion of the road if it illuminates a sufficiently far location.

The results in logarithmic scale emphasize the far field beam pattern properties quantitatively. Before looking at the actual results, the reader should be aware that the shape of the pattern is affected by the "cartographic distortion" introduced by mapping a half-sphere onto a flat surface. For example, for an elevation of 0° (the normal to the surface), all the azimuth points in the range −180°–180° actually represent the same point in space (the tip of the normal), whereas for an elevation of 90° (parallel to the surface) each azimuth degree spans a much larger distance.

Besides showing the gain and the size of the main lobe, we observe that the size of the side lobes changes accordingly, and that the far field pattern includes several peaks and troughs. The number of such peaks and troughs increases with the number of elements. This fact is necessary for the interpretation of the results in the following.

As a final point, we indicate the maximum gains for each of the configurations, as they cannot easily be determined by looking at the graphs. In particular, the maximum gains are roughly 20 dB, 25 dB, and 31 dB for $N_{el} = 625$, 2500, and 10 000, respectively. While such values seem large, they are required to compensate for the heavy path loss that affects mmWave signals. Moreover, we remark that even better performance can be achieved using directional transmissions, as shown in [22].

B. Perfect tracking scenario

This section describes the results for the scenario with perfect tracking. We start by analyzing the path loss and then consider the gain provided by the RIS. Note that results referring to path loss are valid regardless of whether tracking is in place, whereas the effects of tracking will be observed on the gain. Here, instead of computing path losses analytically, we show the values obtained from the simulator, which confirm expectation from the model in [19].

We start by observing the results for the product of distances for both the T and Z scenarios (Fig. 4a and 4c). The plots show the total path loss from the transmitter to the receiver as a function of the length of the last hop of the path (d_2 for the T scenario, d_3 for the Z scenario), for multiple distances of the transmitter from the intersection. The path loss is expressed as a negative value in dB. As expected, the results for the two scenarios are qualitatively the same and they only differ by the amount of path loss introduced by the additional path in the Z scenario. What changes significantly is the absolute value of the path loss. For a single reflection, this goes from a minimum of 170 dB to a maximum of 220 dB, while for a double reflection it ranges between 260 dB and 310 dB. Mathematically, such huge losses are caused by the product of the losses computed for each hop. If we consider the path loss component of Eq. (1), at a reference distance of 1 m, on a dB scale we obtain

$$(N_{RIS} + 1) \cdot 20 \log_{10} \left(\frac{4\pi f}{c} \right). \tag{5}$$

For a frequency of 25 GHz, this means that each reflection adds at least 60 dB of loss. Hence, for single and double reflections we cannot expect less than 120 dB and 180 dB of loss, respectively.

When considering the sum of distances (Fig. 4b and 4d), the loss becomes less extreme, since it is computed as if multiple

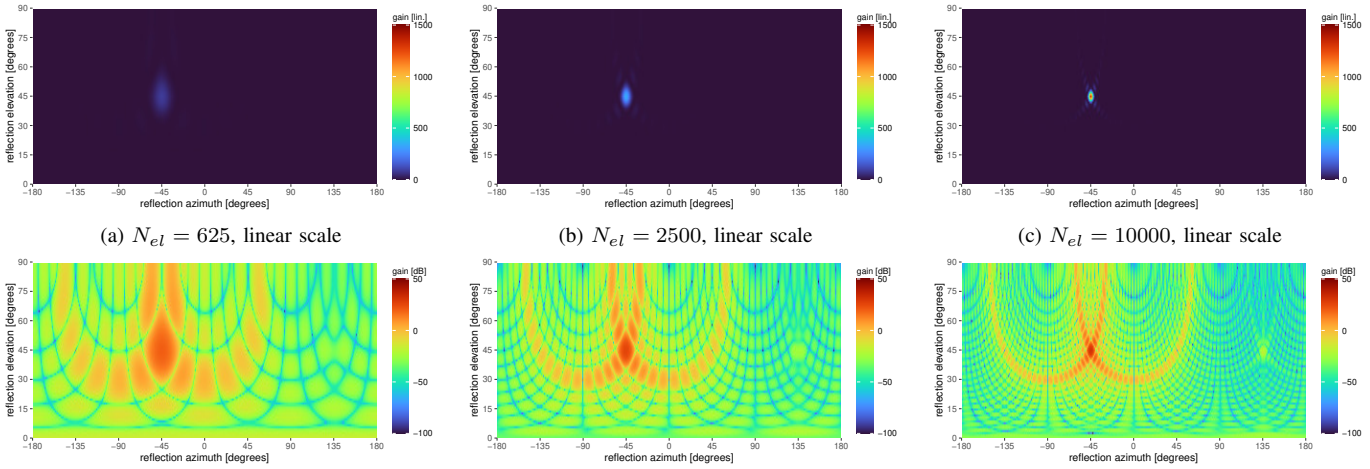

(a) $N_{el} = 625$, linear scale (b) $N_{el} = 2500$, linear scale (c) $N_{el} = 10000$, linear scale

(d) $N_{el} = 625$, dB scale (e) $N_{el} = 2500$, dB scale (f) $N_{el} = 10000$, dB scale

Figure 3. Far field patterns for different number of elements. The RIS is configured for the reflection ($\phi_r = -45°, \theta_r = 45°, \phi_i = 0°, \theta_i = 0°$).

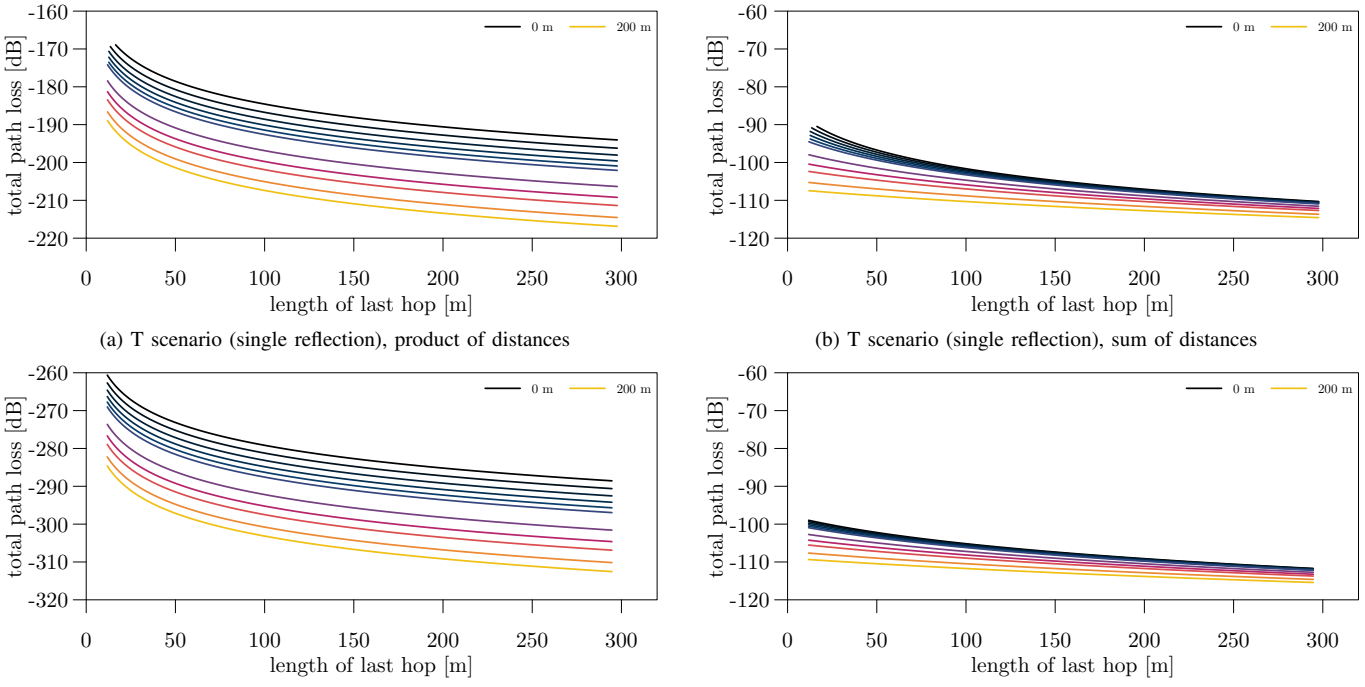

(a) T scenario (single reflection), product of distances (b) T scenario (single reflection), sum of distances

(c) Z scenario (double reflection), product of distances (d) Z scenario (double reflection), sum of distances

Figure 4. Path loss as a function of the last path length (without RIS and antenna gains) measured for single and double reflection, using the sum and the product of distance in the model. Different curves represent the path loss for different distances of the transmitting vehicle from the intersection.

paths were composed into a single one. The impact of the length of the last hop is less evident in this case, as most of the loss occurs over the first hop.

The path loss presented here, however, does not clearly map to the feasibilty of RISs as enablers of mmWave vehicular communications. To help put the values into perspective, we first comment on the noise floor, as it contributes to the signal to noise ratio (SNR), which in turn depends on the bandwidth. For example, for a $10\,\mathrm{MHz}$ channel, the noise floor is roughly $-95\,\mathrm{dBm}$, while for the $400\,\mathrm{MHz}$ typical of a mmWave channel the noise floor can be as high as $-80\,\mathrm{dBm}$. In addition, we have to consider the transmission power and the gains of the antennas (transmitter, receiver, and finally the RISs). By considering a transmission power of $30\,\mathrm{dBm}$ and a noise floor of $-80\,\mathrm{dBm}$, the path loss observed in the plots can easily be translated into a base SNR by shifting the curves up by $110\,\mathrm{dB}$. For the "sum of distances" path loss model, this would already result in an SNR larger than $0\,\mathrm{dB}$, which can be improved by the RIS itself. For the product of distances, the starting SNR would range between $-60\,\mathrm{dB}$ and $-110\,\mathrm{dB}$ for the T scenario and between $-150\,\mathrm{dB}$ and $-200\,\mathrm{dB}$ for the Z scenario.

To further improve the SNR we can consider directional antennas. A dipole antenna can yield $9\,\mathrm{dBi}$ at $2.4\,\mathrm{GHz}$. By

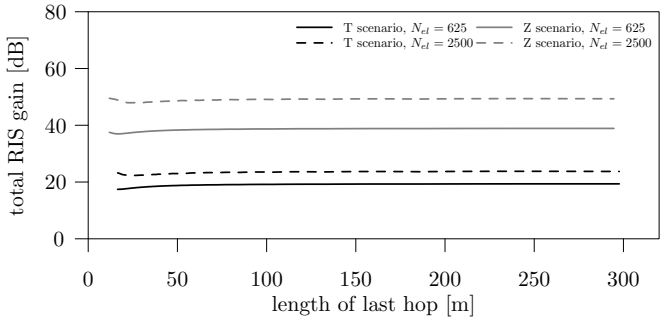

Figure 5. Total RIS gain (over whole path) measured for single and double reflections (T and Z scenarios, respectively), for different number of elements in the RIS when considering perfect tracking.

using the relationship between gain and antenna effective aperture A_e [23], i.e., $G = \frac{4\pi f^2 A_e}{c^2}$ we can compute that the same antenna would provide us with roughly $29\,\mathrm{dBi}$ of gain at $25\,\mathrm{GHz}$, both at the sender and at the receiver. Still, a dipole emits omni-directionally along the plane normal to the dipole itself, whereas a directional antenna pointing towards the RIS would offer higher gain.

The key question is ultimately how much gain the RIS can provide. We partially answered this question in Section IV-A, but these results refer to a specific configuration. We now take a look at the RIS gain with perfect tracking. Fig. 5 shows the total RIS gain as a function of the length of the last hop, for the T and the Z scenarios and for two different numbers of elements. The first fact to notice is the benefit of perfect tracking, i.e., the gain varies negligibly, regardless of the position of the receiving vehicle. Still, the gain for this specific metasurface model and the number of elements considered in the simulation is around $20\,\mathrm{dB}$ to $25\,\mathrm{dB}$ per RIS, which might not be sufficient, especially in the case of multiple reflections. In the latter case, one may decide to consider active surfaces, or models as the one in [22].

C. No tracking scenario

Finally, we consider the case in which the RIS is not tracking the receiver, but it simply illuminates a portion of the road, i.e., pointing $50\,\mathrm{m}$ before the intersection. Fig. 6 shows the gain of the second RIS in the path and the received power as a function of the length of the last hop, for different numbers of elements. With reference to the gain, the graph shows us different facts. First, increasing the number of elements increases the maximum gain and decreases the coverage area, as shown between $50\,\mathrm{m}$ and $100\,\mathrm{m}$. The second fact is that, as we observed in [16], the RIS can provide a positive gain even several hundred meters away from the focal point, at least for a small number of elements. The gain experienced by the receiver after passing the focal point quickly deteriorates because the reflection azimuth and elevation angles change abruptly as the vehicle approaches the intersection (see Fig. 2 for reference). This effect is amplified for larger numbers of elements.

With respect to the coverage in the portion of the road before the focal point, we can see that increasing the number of elements does not lead to a monotonically increasing gain. To explain this effect we refer to Fig. 3, where we observe a larger number of "gain ripples" as we increase the number of elements. Such ripples cause the oscillations in gain that we observe, with a particularly interesting effect on the received power. Considering $N_{el} = 10\,000$, we observe that between $100\,\mathrm{m}$ and $140\,\mathrm{m}$, such configuration provides the highest received power, but between $80\,\mathrm{m}$ and $100\,\mathrm{m}$ the performance is the worst, to then again perform the best close to the focal point. This suggests that, when tracking is disabled, the proper configuration of the RIS is not trivial, and simply increasing the number of elements to achieve the highest possible gain is not necessarily the best solution.

This effect can also be observed by analyzing the received power for the vehicle located on the vertical road of the Z scenario, displayed in Fig. 7. The graphs show the received power as a function of the number of elements of the RIS, for different distances of the transmitter from the intersection. First of all, the received power is higher simply because such vehicle receives the signal after a single reflection. The effects of the gain ripples is apparent: as we increase the number of elements we might expect the received power to decrease monotonically, as the first RIS should focus the signal more and more towards the second RIS. Yet, this is not the case, as the power oscillates before finally decreasing monotonically. This adds an additional level of complexity to the use of RISs in vehicular scenarios: to find a balance between a high gain to reach a primary receiver and a high coverage for non-primary receivers, such aspects would need to be considered for the optimal configuration of the RIS.

V. Conclusions

In this work we perform an initial feasibility study for the use of RISs for V2V in mmWave communications. Our analysis is supported by CoopeRIS, a novel simulation framework for the investigation of cooperative driving systems and RIS-enabled mmWave communications. The results show that in the general case where the total path loss is the product of the path losses over each hop of a wireless path, multiple reflections may easily lead to extremely limited received signal power. Besides directional antennas, RISs can be instrumental in overcoming such losses. Using the RIS model considered in this paper, we observed that seeking higher gains through RIS with more elements leads to non-trivial effects when receivers are not perfectly tracked. As future work, we thus plan to incorporate different RIS models in CoopeRIS to understand the achievable gains and quantify the bandwidth available for V2V communications. In addition, we plan to improve and release CoopeRIS as open source software, especially focusing our effort towards the efficiency of simulations to enable more in-depth studies.

Acknowledgment

This work received support from the European Commission's Horizon 2020 Framework Programme under the Marie Skłodowska-Curie Action MINTS (GA no. 861222).

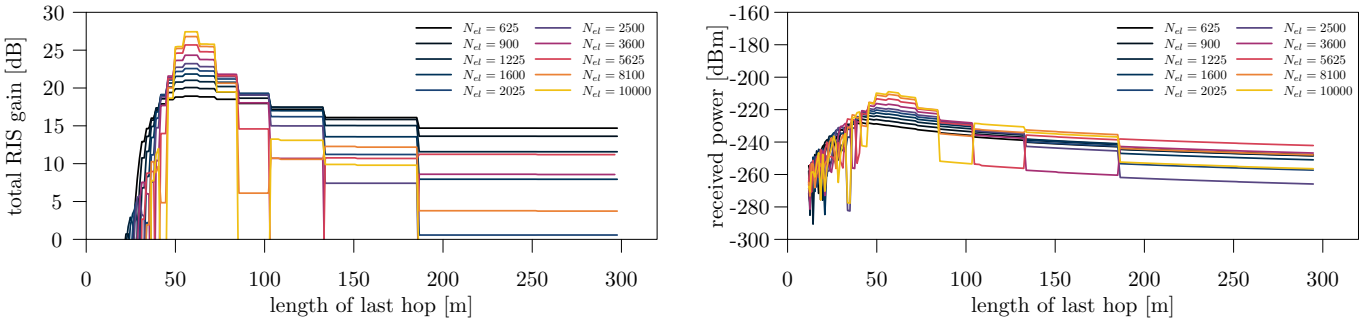

(a) RIS gain (second RIS in the path)

(b) received power (distance to intersection 200 m)

Figure 6. RIS gain and received power for the Z scenario (double reflection) with no tracking and product of distances, for different number of elements in the RIS. The received power refers to the target receiving vehicle.

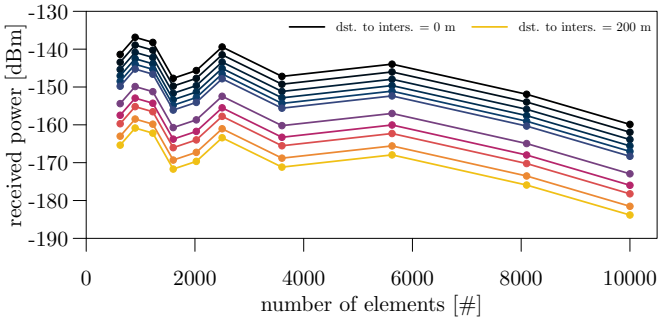

Figure 7. Received power for the Z scenario (double reflection) with no tracking and product of distances as function of the number of elements in the RIS, for different distances of the transmitter from the intersection. The received power refers to the vehicle receiving packet on the second path.

References

[1] V. Lesch, M. Breitbach, M. Segata, C. Becker, S. Kounev, and C. Krupitzer, "An Overview on Approaches for Coordination of Platoons," *IEEE Transactions on Intelligent Transportation Systems (TITS)*, vol. 23, no. 8, pp. 10 049–10 065, Aug. 2022.

[2] H. Wang, Y. Huang, A. Khajepour, Y. Zhang, Y. Rasekhipour, and D. Cao, "Crash Mitigation in Motion Planning for Autonomous Vehicles," *IEEE Transactions on Intelligent Transportation Systems (TITS)*, vol. 20, no. 9, pp. 3313–3323, Sep. 2019.

[3] M. Noor-A-Rahim, Z. Liu, H. Lee, et al., "6G for Vehicle-to-Everything (V2X) Communications: Enabling Technologies, Challenges, and Opportunities," *Proceedings of the IEEE*, vol. 110, no. 6, Jun. 2022.

[4] M. Xiao, S. Mumtaz, Y. Huang, et al., "Millimeter Wave Communications for Future Mobile Networks," *IEEE Journal on Selected Areas in Communications (JSAC)*, vol. 35, no. 9, pp. 1909–1935, Sep. 2017.

[5] C. Liaskos, A. Tsioliaridou, S. Nie, A. Pitsillides, S. Ioannidis, and I. F. Akyildiz, "On the Network-Layer Modeling and Configuration of Programmable Wireless Environments," *IEEE/ACM Transactions on Networking (TON)*, vol. 27, no. 4, Aug. 2019.

[6] S. A. Tegos, D. Tyrovolas, P. D. Diamantoulakis, C. Liaskos, and G. K. Karagiannidis, "On the Distribution of the Sum of Double-Nakagami-m Random Vectors and Application in Randomly Reconfigurable Surfaces," *IEEE Transactions on Vehicular Technology (TVT)*, vol. 71, no. 7, Jul. 2022.

[7] A. Pitilakis, O. Tsilipakos, F. Liu, et al., "A Multi-Functional Reconfigurable Metasurface: Electromagnetic Design Accounting for Fabrication Aspects," *IEEE Transactions on Antennas and Propagation*, vol. 69, no. 3, Mar. 2021.

[8] R. Guirado, G. Perez-Palomino, M. Cano-Garcia, M. A. Geday, and E. Carrasco, "mm-Wave Metasurface Unit Cells Achieving Millisecond Response Through Polymer Network Liquid Crystals," *IEEE Access*, vol. 10, pp. 127 928–127 938, Nov. 2022.

[9] D. Tyrovolas, S. A. Tegos, E. C. Dimitriadou-Panidou, P. D. Diamantoulakis, C. Liaskos, and G. K. Karagiannidis, "Performance Analysis of Cascaded Reconfigurable Intelligent Surface Networks," *IEEE Wireless Communications Letters (WCL)*, vol. 11, no. 9, Sep. 2022.

[10] Y. Zhu, B. Mao, and N. Kato, "Intelligent Reflecting Surface in 6G Vehicular Communications: A Survey," *IEEE Open Journal of Vehicular Technology*, vol. 3, 2022.

[11] Y. Chen, Y. Wang, and L. Jiao, "Robust Transmission for Reconfigurable Intelligent Surface Aided Millimeter Wave Vehicular Communications With Statistical CSI," *IEEE Transactions on Wireless Communications (TWC)*, vol. 21, no. 2, Feb. 2022.

[12] J. Wang, W. Zhang, X. Bao, T. Song, and C. Pan, "Outage Analysis for Intelligent Reflecting Surface Assisted Vehicular Communication Networks," in *IEEE Global Communications Conference (GLOBECOM 2020)*, Taipei, Taiwan, Dec. 2020.

[13] Y. Ai, F. A. P. deFigueiredo, L. Kong, M. Cheffena, S. Chatzinotas, and B. Ottersten, "Secure Vehicular Communications Through Reconfigurable Intelligent Surfaces," *IEEE Transactions on Vehicular Technology (TVT)*, vol. 70, no. 7, Jul. 2021.

[14] Y. U. Ozcan, O. Ozdemir, and G. K. Kurt, "Reconfigurable Intelligent Surfaces for the Connectivity of Autonomous Vehicles," *IEEE Transactions on Vehicular Technology (TVT)*, vol. 70, no. 3, 2021.

[15] T. Saeed, W. Aziz, A. Pitsillides, et al., "On the Use of Programmable Metasurfaces in Vehicular Networks," in *22nd IEEE International Workshop on Signal Processing Advances in Wireless Communications (SPAWC 2021)*, Lucca, Italy, Sep. 2021.

[16] M. Segata, M. Lestas, P. Casari, et al., "Enabling Cooperative Autonomous Driving Through mmWave and Reconfigurable Intelligent Surfaces," in *18th IEEE/IFIP Conference on Wireless On demand Network Systems and Services (WONS 2023)*, Madonna di Campiglio, Italy: IEEE, Jan. 2023.

[17] C. Liaskos, S. Nie, A. Tsioliaridou, A. Pitsillides, S. Ioannidis, and I. F. Akyildiz, "A New Wireless Communication Paradigm through Software-Controlled Metasurfaces," *IEEE Communications Magazine (COMMAG)*, vol. 56, no. 9, Sep. 2018.

[18] M. Segata, R. Lo Cigno, T. Hardes, et al., "Multi-Technology Cooperative Driving: An Analysis Based on PLEXE," *IEEE Transactions on Mobile Computing (TMC)*, Feb. 2022, to appear.

[19] H. Taghvaee, S. Abadal, A. Pitilakis, et al., "Scalability Analysis of Programmable Metasurfaces for Beam Steering," *IEEE Access*, vol. 8, May 2020.

[20] W. Tang, X. Chen, M. Z. Chen, et al., "Path Loss Modeling and Measurements for Reconfigurable Intelligent Surfaces in the Millimeter-Wave Frequency Band," *IEEE Transactions on Communications (TCOM)*, vol. 70, no. 9, Sep. 2022.

[21] C. Sommer, D. Eckhoff, R. German, and F. Dressler, "A Computationally Inexpensive Empirical Model of IEEE 802.11p Radio Shadowing in Urban Environments," in *8th IEEE/IFIP Conference on Wireless On demand Network Systems and Services (WONS 2011)*, Bardonecchia, Italy, Jan. 2011.

[22] D. Tyrovolas, S. A. Tegos, P. D. Diamantoulakis, and G. K. Karagiannidis, "Synergetic UAV-RIS Communication With Highly Directional Transmission," *IEEE Wireless Communications Letters (WCL)*, vol. 11, no. 3, pp. 583–587, Mar. 2022.

[23] T. S. Rappaport, *Wireless Communications: Principles and Practice*, 2nd ed. Upper Saddle River, NJ: Prentice Hall, 2001.